Direct Observation of the Geometry of Atom−Atom and Atom−Molecule Collisions

J. Grosser,* O. Hoffmann, and C. Rakete

Institut für Atom- und Molekülphysik, Universität Hannover, 30167 Hannover, Germany

F. Rebentrost

Max-Planck-Institut für Quantenoptik, 85748 Garching, Germany

Received: March 11, 1997; In Final Form: May 23, 1997[⊗]

We report crossed beam experiments on the laser assisted collisions Na(3s) + M + $h\nu$ → Na(3p) + M with M = Kr, N_2, and CO_2. By varying the photon polarization, we gain direct insight into the geometric properties of the collision complex. For the Na + Kr system, we are able to deduce from the experimental data the two possible directions (Condon vectors) of the internuclear axis at the moment of the optical transition.

1. Introduction

Atomic and molecular collisions have been and are being studied experimentally in many laboratories. With very few exceptions, the experimental effort is concentrated on the preparation of the colliding particles and on the study of the collision products. Experiments of this type can have the form of very detailed studies, involving the use of atomic or molecular beams and angle-resolved detection, and of sophisticated methods for the preparation and the analysis of atomic and molecular states. The results are often used to discuss the collision event itself; the information gained in this way about the mechanism of a collision is necessarily indirect and therefore more or less uncertain.

The absorption of light by a system of colliding particles provides a possibility for the direct study of collisions.[1] Experiments of this type have been performed for atom−atom,[2−5] atom−molecule,[6] and even chemically reactive collisions.[7−9] Photodissociating ("half-collision") systems have been studied with femtosecond laser pulses[10] in many cases. The last group of experiments is capable of providing direct insight into the time evolution of atomic systems. Direct experimental insight into the geometric structure of a collisional event has however not been achieved so far. In contrast to all previous experiments, the present studies use atomic beams and an angle-resolved detection scheme. We will demonstrate that this makes geometrical properties of the collision complex observable.

We have demonstrated[11−15] that crossed beam experiments on laser assisted ("optical") atom−atom collisions,

$$A + M + h\nu \rightarrow A^* + M \qquad (1)$$

where the photon energy $h\nu$ is detuned with respect to the atomic A−A* transition energy, offer unprecedented possibilities for observing collision processes and for investigating the underlying molecular interactions. Especially, polarization experiments have been shown to give direct access to the geometric properties of the collision complex AM. The purpose of the present paper is to demonstrate (1) that, for an atom−atom collision, a very detailed insight into the geometry of the collision complex can be obtained and (2) that the method yields valuable, though less detailed, information for atom−molecule collisions also.

2. Experimental Method

The experiment has been described previously.[11,12] We therefore summarize here only the most important aspects. Figure 1 shows the experimental setup. A thermal Na atom beam, a pulsed nozzle target beam, and two laser beams intersect each other in the scattering volume. One of the laser beams ("excitation" laser) has a photon energy close, but not identical, to the Na(3s → 3p) transition energy. Two atoms and one such photon can interact to produce an excited atom:

$$Na(3s) + M + h\nu \rightarrow Na(3p) + M \qquad (2)$$

We express the photon wavenumber by the detuning $\Delta\nu/c = (\nu - \nu_{res})/c$, with ν_{res} corresponding to the Na D_1 ($3s \rightarrow 3p_{1/2}$) transition. Typically, the detuning is of the order of ± 100 cm^{-1}. In order to allow a differential detection, the Na(3p) collision products are transferred to a Rydberg state by the second ("detection") laser. The Rydberg atoms live long enough to travel to a rotatable distant detector, where they are field-ionized and finally counted. The velocity of the products is obtained by a time-of-flight measurement. In the atom−atom case, we obtain the full kinematic information in this way; i.e. for every particle detected, we know all velocity vectors before and after the optical collision within narrow limits. We know, especially, the relative velocity vectors $\mathbf{v} = \mathbf{v}_{Na} - \mathbf{v}_M$ before and after the collision. These vectors are of special interest, because they indicate the direction of the Na−M axis before and after the collision. For the atom−molecule collisions, the amount of vibrational or rotational energy transfer is not known. We do not observe large energy losses of the Na atoms, however, and will therefore at present simply disregard vibrational and rotational energy transfer. This means, however, that we possess only a qualitative knowledge of the kinematics, especially of the relative velocity vectors, in these cases. In the NaKr case, the resolution for the center-of-mass scattering angle is typically 4° full width at half-maximum (fwhm). This is representative for the atom−molecule cases as well. The relative velocity can be resolved within 60 m/s fwhm. Some of the measurements reported here were carried out with a lower velocity resolution. The target beam has a thermal velocity distribution; the velocity spread corresponds to a translational temperature of about 50 K for the molecular targets and 6 K for the atomic target. The molecules are in their vibrational ground states, but a number of rotational states is certainly populated. The detection laser is operated on a Na($3p_{1/2} \rightarrow nd$) transition with n between 30 and 40 and is linearly polarized.

[⊗] Abstract published in *Advance ACS Abstracts,* September 15, 1997.

S1089-5639(97)00904-3 CCC: $14.00

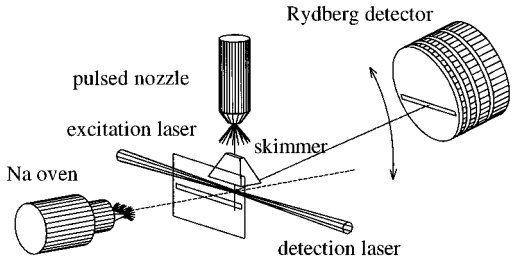

Figure 1. Principle of the experimental setup with two particle beams, two counterpropagating laser beams, and a rotatable detector.

The signal is then strictly proportional to the population of the $3p_{1/2}$ state, independent of a possible orientation.[16] We use nanosecond laser pulses. They are long compared to the picosecond duration of the collision. This means that the lasers are on during the entire optical collision and that the detection process occurs long after the collision, on average.

3. Polarization Experiments and Collisional Geometry

3.1. General. For atom−atom optical collisions, the motion of the nuclei can be discussed in terms of classical trajectories. For the NaKr system, this is close to exact, provided that interference effects are duely taken into account.[14] We use the classical trajectory interpretation throughout this paper. The optical transition, which occurs during the collision, is restricted to those configurations of the collision complex, for which the resonance condition

$$V_f(\mathbf{r}) - V_i(\mathbf{r}) = h\nu \tag{3}$$

is fulfilled. V_i and V_f are the ground and excited state potential energy surfaces, $\mathbf{r}$ is the complete set of nuclear coordinates, and $h\nu$ is the photon energy. For a single trajectory $\mathbf{r} = \mathbf{r}(t)$, the transition occurs normally at a single, well-defined configuration $\mathbf{r}_c$. We call this the Condon configuration for the trajectory considered. The optical transition probability is, in the dipole approximation, proportional to $|\sum_\nu \langle f|d_\nu|i\rangle E_\nu|^2$. $\langle i|$ and $\langle f|$ are the initial and final electronic wave functions for the nuclear configuration $\mathbf{r}_c$, and d_ν and E_ν are the Cartesian components of the electronic dipole operator and of the electric field vector (we consider only linear polarization at the moment). The matrix elements $\langle f|d_\nu|i\rangle$ form a vector (the transition dipole), which depends on $\mathbf{r}_c$. There are usually signal contributions from more than one trajectory, which must be added coherently. The signal intensity is then

$$I = |\sum_\alpha c_\alpha \sum_\nu \langle f|d_\nu|i\rangle E_\nu|^2 \tag{4}$$

The label α enumerates the different trajectories. For the atom−atom case, explict expressions for the complex amplitudes c_α can be found in ref 14. Depending on the complexity of the system, α can be discrete or continuous; the $\sum_\alpha$ becomes an integral in the latter case. Most generally, the experimental signal can be an incoherent sum of contributions of the form of eq 4, e.g. when a target molecule is present in different rotational states. The signal intensity has always the general form

$$I = \sum_{\mu\nu} A_{\mu\nu} E_\mu E_\nu \tag{5}$$

with a field-independent tensor $\mathbf{A}_{\mu\nu}$. Like every symmetric tensor, $\mathbf{A}_{\mu\nu}$ can be characterized by its main axes. For the symmetry conditions of the present experiment, two of the main axes are in the scattering plane in Figure 1 and one is at right angles. As the polarization vector $\mathbf{E}_\nu$ is in the scattering plane

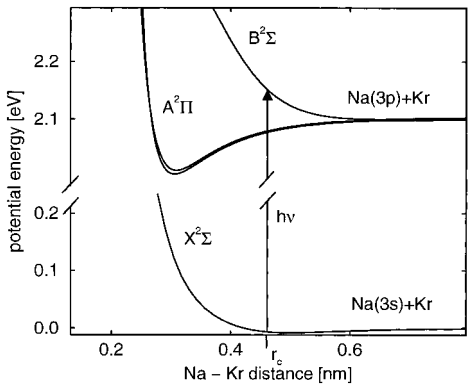

Figure 2. Potential curves of the NaKr collisional molecule. The arrow represents the photon energy $h\nu$ of the excitation laser. The optical transition is limited to a small range of internuclear distances around the value r_c, where the photon is resonant.

as well, the signal intensity can be expressed as

$$I = A'_{11}(E'_1)^2 + A'_{22}(E'_2)^2 \tag{6}$$

The Cartesian components E'_i refer now to the directions of the main axes; the sum extends only over the axes in the scattering plane. The geometric properties of $\mathbf{A}_{\mu\nu}$ are easily obtained from polarization experiments; e.g., the main axis with the largest main value corresponds to the polarization direction, for which the largest signal intensity is observed. We designate the quantity $\mathbf{A}_{\mu\nu}$ as the alignment tensor of the transition dipole moments. Alignment tensors are a well-known tool for characterizing the wave functions of an ensemble of isolated atoms,[16] and the alignment of atomic collision products has been measured in many cases.[17,18] The tensor $\mathbf{A}_{\mu\nu}$, which we use here, is closely related to this notion, and the experimental methods, which we use to measure its geometric properties, are identical. Unlike the old concepts, $\mathbf{A}_{\mu\nu}$ describes a property of the collision complex, however, and not a property of a collision product.

An important simplification arises, when all signal contributions can be added incoherently. Then

$$\mathbf{A}_{\mu\nu}\ \mathrm{Re} \sum_\alpha p_\alpha \langle f|d_\nu|i\rangle \langle f|d_\mu|i\rangle^* \tag{7}$$

where p_α is the weight factor of the α th signal contribution, e.g. $p_\alpha = |c_\alpha|^2$. In this case, $\mathbf{A}_{\mu\nu}$ simply characterizes the statistical distribution of the transition dipoles, which contribute to the experimental signal.

We use the NaKr case at a positive detuning to illustrate the general considerations. Figure 2 shows the NaKr potential curve system.[19,20] For positive detuning, only the repulsive $B^2\Sigma$ state can be excited. The resonance condition eq 3 is fullfilled when the atoms are at the distance r_c, the "Condon radius". Figure 3 shows numerically computed classical trajectories. The vectors $\mathbf{r}_1$ and $\mathbf{r}_2$ ("Condon vectors") mark the points on the trajectories where the optical transition takes place; the relative position of the two atoms corresponds to one or the other of the Condon vectors at the instant of the transition. For NaKr and a positive detuning, there are only two trajectories which lead to a given scattering angle. In the first case, the transition occurs at the first passage of the trajectory through the circle with radius r_c; in the second case, at the second passage. Note that the first trajectory cannot have the transition at the second passage and vice versa: the force inside the circle would be different, leading to a different deflection. The set of Condon configurations consists here only of the two members $\mathbf{r}_1$ and $\mathbf{r}_2$. Correspond-

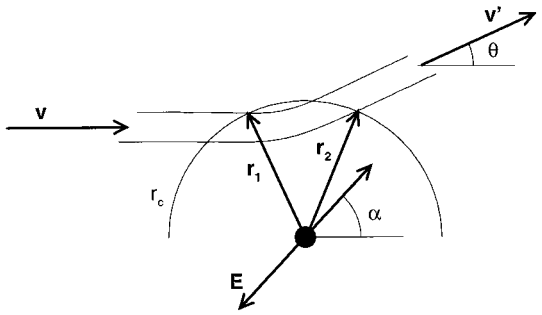

Figure 3. Collisional geometry of the NaKr optical collision for a positive detuning. The curves are the classical trajectories for the vector **r** between the two atoms. The half-circle shows the Condon radius r_c; the Condon vectors $\mathbf{r}_1$ and $\mathbf{r}_2$ mark the points on the trajectories, where the optical transition occurs. **E** indicates the variable polarization of the excitation laser. **v** and **v′** are the relative velocity vectors before and after the collision; θ and α measure the center-of-mass scattering angle and the polarization direction, respectively.

ingly, the $\sum_\alpha$ in eqs 4 and 7 goes only over two terms. As the transition is between two molecular Σ states, the transition dipole moment has the direction of the internuclear axis. For incoherent superposition, the signal intensity is found from eqs 5 and 7:

$$I = p_1(\mathbf{r}_1 \cdot \mathbf{E})^2 + p_2(\mathbf{r}_2 \cdot \mathbf{E})^2 \tag{8}$$

This is easily converted into expressions for the main axes and main values of the alignment tensor. For instance, the major axis (the polarization direction with the largest signal intensity) is found at the angle

$$\alpha = q_1\alpha_1 + q_2\alpha_2 \tag{9}$$

where α_1, α_2 are the angles of the Condon vectors, all angles are measured with respect to an arbitrary direction, and

$$q_1 + q_2 = 1, \quad \frac{q_1}{q_2} = \frac{\operatorname{arccot}[(p_2/p_1 + \cos(2\Delta\alpha))/\sin(2\Delta\alpha)]}{\operatorname{arccot}[(p_1/p_2 + \cos(2\Delta\alpha))/\sin(2\Delta\alpha)]} \tag{10}$$

$\Delta\alpha = \alpha_1 - \alpha_2$ is the angle between the Condon vectors. Accordingly, the direction of the large main axis of $\mathbf{A}_{\mu\nu}$ is a weighted average of the directions of the Condon vectors. Equation 10 has the property to enhance the weight of the larger one of the two contributions; maximum signal intensity occurs for a polarization angle, which is closer to the more prominent Condon vector than $(p_1\alpha_1 + p_2\alpha_2)/(p_1 + p_2)$.

Equations 7−10 hold only as long as the signal contributions can be added incoherently. This seems reasonable, at least as a first approach, for the atom−molecule systems. In the NaKr case at positive detuning, the differential cross-sections show oscillations which are due to the interference of the two signal contributions (see Figure 6 below). The experimental directions of the main axes do not show any corresponding variation. This justifies the use of eqs 9 and 10. The experimental main values (A'_{11} and A'_{22} in eq 6) show slight interference structures; the data, which we present in the following section, have been averaged over an oscillation period. For NaKr at a negative detuning, we observe no interference; i.e., the incoherent interpretation is applicable in this case as well. The interaction of polarization and interference will be considered in section 3.3.

3.2. Alignment: Experimental Results and Interpretation. In Figure 4, we present experimental results for the alignment tensor. The arrows indicate the directions of the relative velocity vectors $\mathbf{v} = \mathbf{v}_{Na} - \mathbf{v}_M$ before and after the collision, where M denotes the second collision partner. They show, at the same time, the directions of the Na−M axis long before and long after the collision. The dots are the original experimental data; they show the signal intensity as a function of the linear polarization direction in a polar diagram. The bars give the main axes of the alignment tensors; they were derived from the intensity distribution by a numerical fit to eq 6. Generally, the results show a considerable variability, indicating a great sensitivity of the experimental data on the details of the process.

Figure 5 compares the experimental data for NaKr with theoretical results. The bars are the experimental alignment tensors. The curves are classical trajectories, which were computed numerically. The circles show the calculated Condon points, and their diameter represents the weight factor $p(\mathbf{r}_c)$; p was computed as in ref 14. Figure 5a refers to a positive detuning. The experimental results for the large main axis are between the Condon vectors, as expected from eq 9. They are not just their arithmetic mean because p_1 and p_2 and, even more, q_1 and q_2 are different. Note that the direction of the Condon vectors varies with the scattering angle. This is reproduced by the experimental results, demonstrating that the experimental data provide a direct, simple, and realistic image of the geometric properties of the collision complex. Figure 5b refers to a negative detuning. In this case there are contributions from four trajectories. However, only the two with the largest weight are of practical importance for the alignment tensor. Since now a Π state is excited (Figure 2), the transition dipole is at right angles to the NaKr axis. The major axis of the alignment tensor is therefore expected to be essentially at right angles to the dominant Condon vectors. This is indeed observed. Note that the method is sensitive to the direction **r** of a Condon vector, but does not distinguish between $+\mathbf{r}$ and $-\mathbf{r}$.

For the atom−molecule systems, the relation between the experimental data and the collision geometry is less direct. This is because there is generally a larger set of Condon configurations and because the relation between the arrangement of the atoms and the direction of the transition dipole is not as simple as that in the atom−atom case. The N_2 data for positive detuning nonetheless have considerable similarity with the corresponding Kr results, whereas the corresponding CO_2 data are quite different. We will give a tentative explanation. The energy of the exciting photons is close to the Na(3s→3p) transition energy. The optical transition is therefore essentially from a Na(3s) to a Na(3p) state in all cases studied here. The transition dipole has the same direction as the 3p molecular orbital, which is excited by the transition. For the NaKr $B^2\Sigma$ and $A^2\Pi$ states, the orbital and correspondingly the transition dipole are aligned, respectively, along or at right angles to the internuclear axis. This has already been used for the interpretation of the NaKr data. The N_2 molecule has only closed molecular orbitals and behaves therefore like a noble gas atom in many aspects. It has no static dipole moment and only a small quadrupole moment.[21] This suggests that the Na−N_2 interaction is essentially a central interaction. The molecular eigenstates then have the Na(3p) orbital aligned along or at right angles to the Na−N_2 axis (Σ- or Π-like states, respectively). The CO_2 molecule has lone pair electrons at the oxygen atoms; this leads to a negative charge at the two oxygens and a positive one at the carbon and hence to a large quadrupole moment.[21] We expect the Na−CO_2 interaction to be dominated by this charge distribution. The alignment of the Na(3p) orbital in the $NaCO_2$ molecular eigenstates is then governed by the direction of the CO_2 axis, and not by that of the Na−CO_2 axis. In the NaKr and NaN_2 cases, the alignment tensor reflects the statistical distribution of the axis connecting the collision partners in the

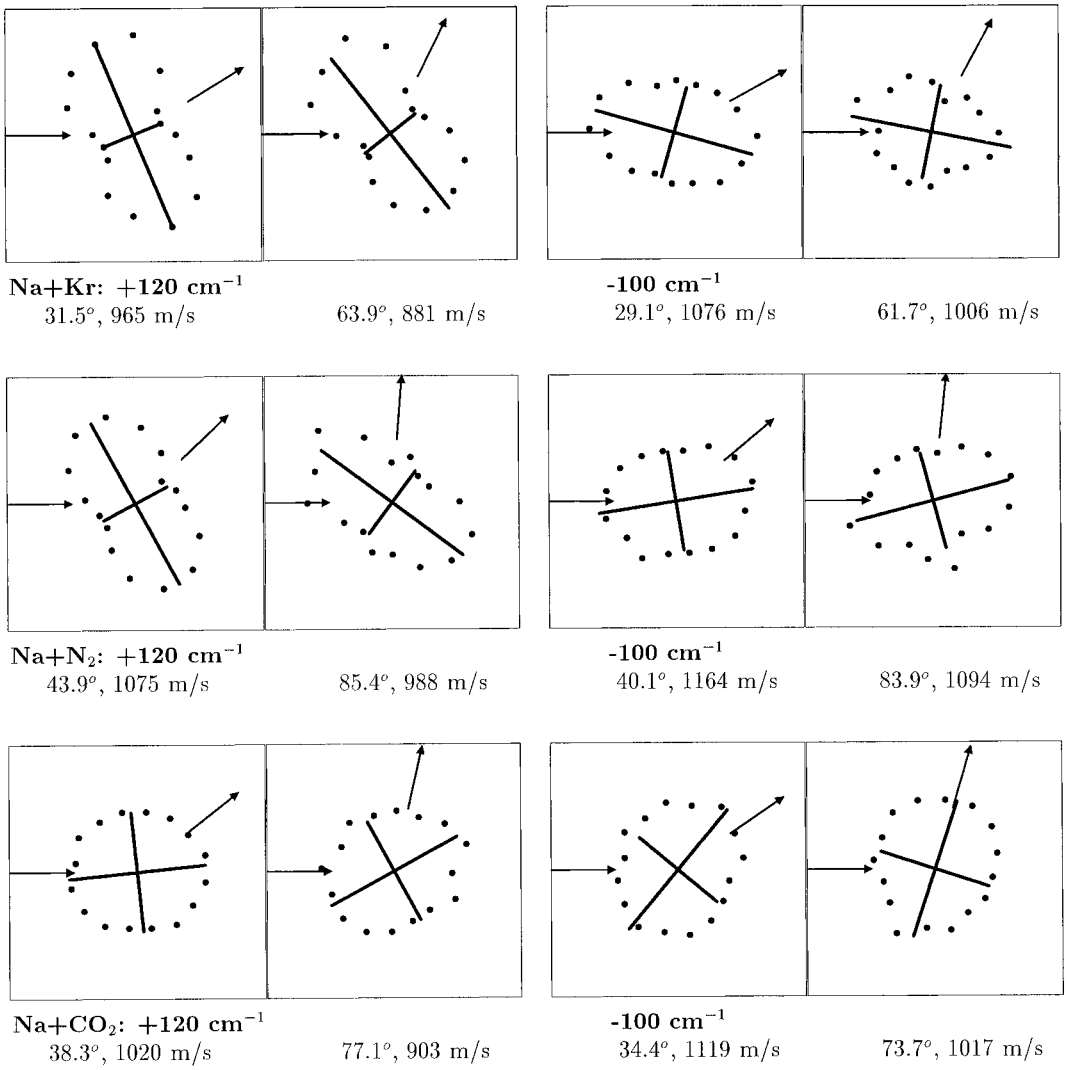

Figure 4. Experimental results. The collision pair, detuning, center-of-mass scattering angle, and relative velocity are indicated below the figures. The dots show the dependence of the signal intensity on the laser polarization in a polar diagram; the bars are the corresponding main axes of the alignment tensor $\mathbf{A}_{\mu\nu}$. The arrows represent the directions of the relative velocity before and after the collision.

moment of the transition, e.g. as in Figure 5; this can explain the similarity between the Kr and N_2 results. In the CO_2 case, the alignment tensor rather reflects the statistical distribution of the molecular axis of the collision partner CO_2 in the moment of the transition. The experimental alignment tensors in this case are close to isotropic, because the CO_2 axes have an isotropic or close to isotropic distribution.

3.3. Geometric Information from Interference Structures. When interference structures are resolved, the alignment tensor will no longer have the simple geometric meaning expressed by eqs 7−10. Interference structures can however be used to gain even more insight into the geometric properties of the collisional system. Figure 6a shows differential cross-sections for the Na(3p) atoms from the Na + Kr process at a positive detuning. The oscillations ("Stueckelberg" oscillations) are caused by the interference of the contributions from the two trajectories (Figure 3). The structures vary with the polarization of the excitation laser; see Figures 6b,c.

Figure 7 shows Stueckelberg oscillations computed for different directions of the linear polarization (positive detuning). The small graphs at the right hand side show computed trajectories and Condon vectors for the same conditions. They belong to a scattering angle of 27°, and they are identical in all polarization cases. In addition, the small graphs show the polarization vector. One observes that the Stueckelberg oscillations vanish when the polarization is at right angles to one of the Condon vectors. The reason is obvious. As we excite a Σ state, the signal contribution from a single Condon point is proportional to $(\boldsymbol{r}_c \cdot \mathbf{E})^2$. When $\mathbf{E}$ is at right angles to a Condon vector, there remains only one signal contribution, and hence there is no interference any more. Between the two directions with vanishing oscillations, the oscillations are inverted. The data in Figure 6b were obtained with polarization directions for which we expect normal and inverted oscillations, respectively. Figure 8a shows, for the same experimental conditions as those in Figure 6b, the contrast $(I_{max} - I_{min})/(I_{max} + I_{min})$ of the Stueckelberg oscillations as a function of the polarization angle. The contrast was evaluated for one oscillation period, using $I_{min} = I(\theta_{min})$ and $I_{max} = [I(\theta_{max1}) + I(\theta_{max2})]/2$; θ_{min}, θ_{max1}, and θ_{max2} are indicated in Figure 6b. In this way, a negative contrast means an inverted oscillation. The solid curve in Figure 8a is a polynomial fit to the experimental points. Its zeros indicate the polarization directions where the oscillations vanish and hence the directions of the two Condon vectors. These directions are shown in Figure 8b, together with corresponding theoretical data. The agreement between experiment and theory is satisfactory. We have no doubt that it can be considerably improved, when the experiments are performed with better angular resolution, or when a refined method of evaluation is applied.

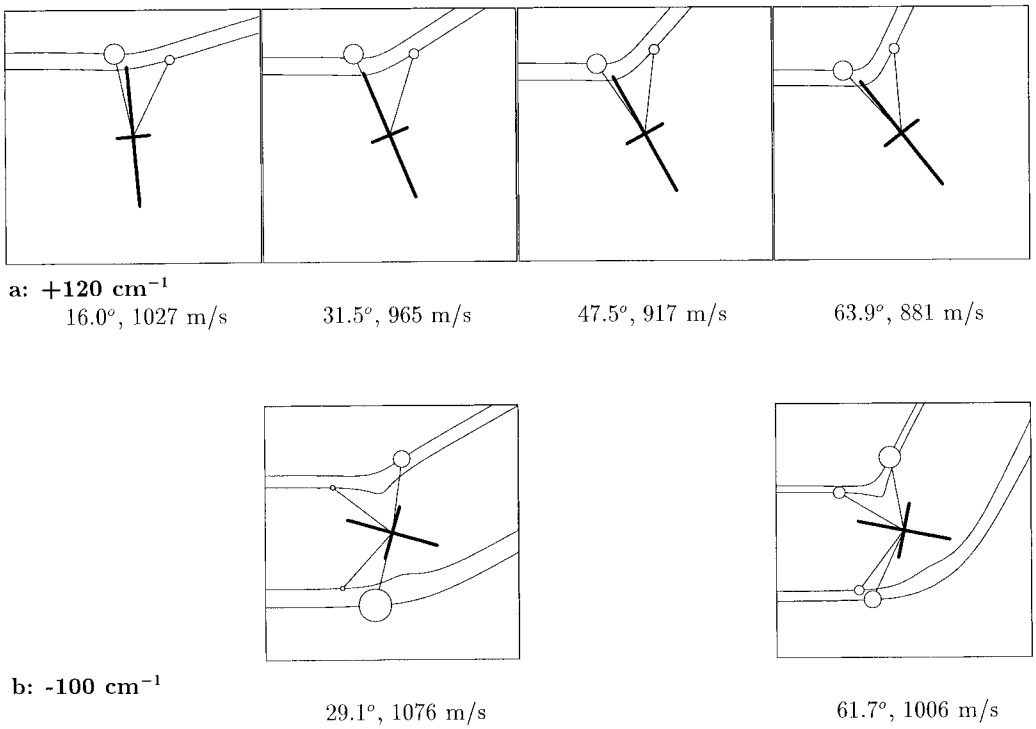

Figure 5. Comparison of experimental and theoretical results for the NaKr system for (a) positive and (b) negative detuning. The numbers below the figures indicate the center-of-mass scattering angles and the relative velocities. The bars show the experimental main axes of the alignment tensor $\mathbf{A}_{\mu\nu}$. The curves are the calculated trajectories. The circles mark the Condon points; the diameter is proportional to their statistical weight.

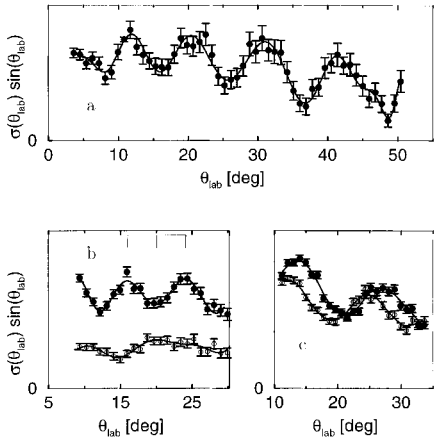

Figure 6. (a) Typical angular distribution of the Na(3p) atoms from the NaKr optical collision: detuning, 120 cm^{-1}; velocity v_{Na} of the collision products, 1091 m/s. The structures are interference (Stueckelberg) oscillations. (b) Stueckelberg oscillations for two different linear polarization directions: detuning, 80 cm^{-1}; v_{Na}, 1212 m/s. One curve shows normal and the other one inverted oscillations. The angles θ_{max1}, θ_{min}, and θ_{max2}, which were used for the evaluation of the contrast, are indicated. (c) Stueckelberg oscillations for left and right circular polarization: detuning, 288.5 cm^{-1}; v_{Na}, 1137 m/s. The interference patterns are shifted with respect to each other.

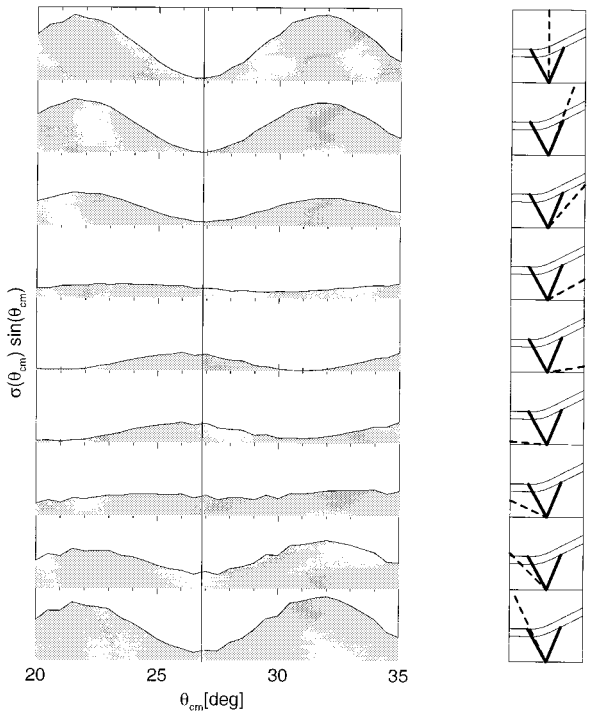

Figure 7. Theoretical differential cross-sections for NaKr for different directions of the linear polarization: full quantum mechanical calculations;[14] detuning, 80 cm^{-1}; relative velocity, 1125 m/s. The small graphs show the classical trajectories and the Condon vectors for a scattering angle of 27° (corresponding to the vertical line in the large graph); in addition, the small graphs show the polarization direction as a dashed line. The interference oscillations vanish when the polarization is at right angles to one of the Condon vectors; this corresponds, approximately, to the fourth and seventh rows.

The oscillation patterns for left and right circular polarization (Figure 6c) are shifted with respect to each other. In the framework of semiclassical theory,[14] this is easily shown to be due to an additional phase shift

$$\Delta\Phi = 2(\alpha_1 - \alpha_2) \tag{11}$$

with $\alpha_1 - \alpha_2$ being the angle between the Condon vectors. Figure 9 shows angles $\alpha_1 - \alpha_2$, which were derived in this way from experiments with right and left circular polarization, together with a corresponding classical numerical result. The agreement again is very satisfactory.

4. Discussion

Optical collisions have been studied and used as a tool for the investigation of molecular interactions over the past 25

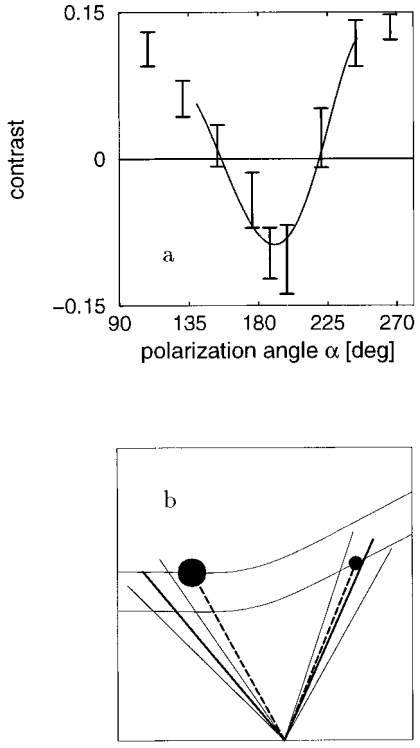

Figure 8. (a) Contrast $(I_{max} - I_{min})/(I_{max} + I_{min})$ of the Stueckelberg oscillations for NaKr as a function of the polarization direction: detuning, 80 cm^{-1}; center-of-mass scattering angle, 27°; relative velocity, 1125 m/s. The polarization angle α has the same meaning as in Figure 3. The line is a polynomial fit. (b) Directions of both Condon vectors: solid straight lines, experimental result and error margins derived from the zeros in a. Solid curves, theoretical classical trajectories, dashed lines, theoretical Condon vectors (the diameter of the circles shows the weight of the Condon points).

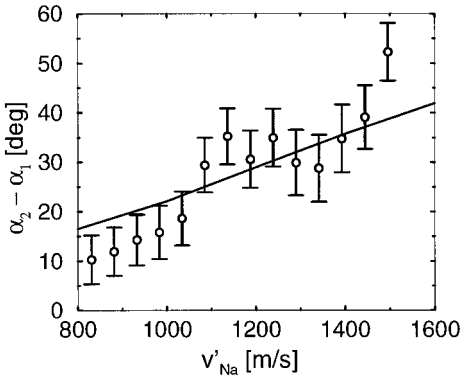

Figure 9. Bars: experimental results for the angle between the Condon vectors obtained from circular polarization experiments. Solid line: classical theoretical result. Detuning, 288.5 cm^{-1}; center-of-mass scattering angle, 31°.

years.[1−6] These studies were always undertaken in the form of gas cell experiments. In the present experiment, the relative velocity vectors before and after the collision are fixed in space, the first one by the use of beams, the second one by the use of a differential detector. As a consequence, the collisional geometry is fixed in space, as well. For the NaKr case, Figures 3 and 5 demonstrate how the Condon vectors have a fixed direction in space because **v** and **v′** do. It is in this way that the geometry of the collision complex becomes experimentally accessible. In contrast one has an isotropic distribution of both **v** and **v′** under the conditions of a gas cell experiment and hence an isotropic distribution of the Condon configurations and transition dipoles.

In a beam experiment with integral detection, one expects a broad, but not necessarily isotropic, distribution for the transition dipole. Integral beam experiments are already capable of yielding geometric information similar to the present results. The use of a differential detector however makes the experiments much more sensitive, because only a small number of trajectories contributes to the signal. We have been working with two trajectories in the most favorable case (Figure 5a). We have demonstrated, in addition, that the analysis of interference structures can yield geometric information, which is related to a single trajectory only. The technique used for this latter purpose can, in principle, be extended to more complicated cases; for instance, the separate determination of the four Condon vectors, which characterize the NaKr system at a negative detuning, should be possible in this way. For atom−molecule collisions, there is an infinity of contributing trajectories **r**(*t*) and hence Condon configurations, even with differential detection, because the motion of the target molecules is not sufficiently controlled. A number of modifications of the present experiment can be envisaged in order to improve this aspect. An experimental control of the internal degrees of freedom of the molecule (by an energy loss analysis or by state selective detection) is the most straightforward approach. The discussion at the end of section 3.2 shows that experiments with spatially oriented molecules are even more desirable.

We use the excitation photon in our experiments to probe a heavy particle collision. The geometric quantities, which we observe, are primarily related to the probing process and not to an unmodified collision. The question arises, whether the present experiments can be extended to make the unmodified evolution of a collision visible. This is indeed possible by pulse−probe experiments. Consider Figure 3 as the simplest example. The excitation process prepares the collision pair in a well-defined molecular state. By using an adequate linear polarization, it is even possible to select a single starting value **r**(0) and a single trajectory **r**(*t*). A second photon can be used to probe the collision at some later time. Polarization experiments can yield geometric information about the collision complex in the moment of the probing transition, quite similar to the information obtained in the present experiments. Probing can be achieved in different ways:

(1) Preparation and probing occur without explicit time resolution (e.g. with nanosecond laser pulses as in the present experiment), and the probing process uses a resonance transition of a free atom or molecule. One observes the result of the evolution from the collision complex to the free products after the collision. Experiments of this type have been realized as gas cell experiments (optical collision experiments with final state analysis).[4,5]

(2) This is similar, but the probing process uses photons detuned from the resonance. Probing occurs then at a moment during the collision which is determined by the detuning. One observes the result of the undisturbed evolution of the collision between the preparation and the probing process. By variation of the probe wavelength and hence the time delay between preparation and probing, the evolution of the collisional geometry with time becomes experimentally accessible. This has also been realized in gas cell experiments (fractional collisions[22]).

(3) Preparation and probing occur with ultrashort light pulses. One observes the evolution of the collision geometry as a function of the delay time. Again, this has been realized in gas cell experiments (time resolved half-collision experiments[10]).

Gas cell experiments do not give access to the collisional geometry. It will therefore be necessary to run these experi-

ments as beam experiments with a differential detection. A first step has already been taken: We have used the detection laser in the present setup as a tool for the product analysis in the NaKr optical collision.[13,20] This belongs to the first group of experiments discussed above. Differential scattering experiments belonging to the second or third groups can give much more insight into the collision dynamics. It appears that the combination of existing experimental techniques with the new methods described in this paper should give us the ability, ultimately, to produce time resolved geometric images of collisions.

Acknowledgment. Financial support from the Deutsche Forschungsgemeinschaft is gratefully acknowledged.

References and Notes

(1) Kleiber, P. D.; Stwalley, W. C.; Sando, K. M. *Annu. Rev. Phys. Chem.* **1993,** *44*, 13−35.

(2) Hedges, R. E. M.; Drummond, D. L.; Gallagher, A. *Phys. Rev. A* **1972**, *6* , 1519−44.

(3) Behmenburg, W.; Makonnen, A.; Kaiser, A.; Rebentrost, F.; Staemmler, V.; Jungen, M.; Peach, G.; Devdariani, A.; Tserkovnyi, S.; Zagrebin, A.; Czuchaj, E. *J. Phys. B* **1996**, *29*, 3891−910.

(4) Havey, M. D.; Delahanty, F. T.; Vahala, L. L.; Copeland, G. E. *Phys. Rev A* **1986**, *34*, 2758−66.

(5) Behmenburg, W.; Ermers, A.; Rebentrost, F. *Z. Phys. D* **1991**, *18*, 93−9.

(6) Ohmori, K.; Kurosawa, T.; Chiba, H.; Okunishi, M.; Ueda, K.; Sato, Y.; Nikitin, E. E. *J. Chem. Phys.* **1995**, *102*, 7341−50.

(7) Raiche, G. A.; Belbruno, J. J. *Chem. Phys. Lett.* **1988**, *146*, 52−7.

(8) Bililign, S.; Kleiber, P. D.; Kearney, W. R.; Sando, K. M. *J. Chem. Phys.* **1992**, *96*, 218−29.

(9) Barnes M. D.; Brooks P. R.; Curl, R. F.; Harland, P. W.; Johnson, B. R. *J. Chem. Phys.* **1992**, *96*, 3559−68.

(10) Kundkhar, L. R.; Zewail, A. H. *Annu. Rev. Phys. Chem.* **1990**, *41*, 15−60.

(11) Grosser, J.; Gundelfinger, D.; Maetzing, A.; Behmenburg, W. *J. Phys. B* **1994**, *27*, L367−73.

(12) Grosser, J.; Hohmeier, D.; Klose, S. *J. Phys. B* **1996**, *29*, 299−306.

(13) Grosser, J.; Hoffmann, O.; Klose, S. In *AIP Conference Procedings 386: Spectral Line Shapes*; AIP Press: New York, 1997; Vol. 9, pp 181−94.

(14) Rebentrost, F.; Klose, S.; Grosser, J. *Z. Phys. D*, submitted for publication.

(15) Grosser J.; Klose, S.; Hoffmann, O.; Rebentrost, F. *Europhys. Lett.* **1997**, *39*, 147−52.

(16) Blum, K. *Density Matrix Theory and Applications;* Plenum Press: New York, 1981.

(17) Andersen, N.; Gallagher, J. W.; Hertel, I. V. *Phys. Rep.* **1988**, *165*, 1−188.

(18) Andersen, N.; Broad, J. T.; Campbell, E. E. B.; Gallagher, J. W.; Hertel, I. V. *Phys. Rep.* **1997**, *278*, 107−289.

(19) Brühl, R.; Kapetanakis, J.; Zimmermann, J. *Chem. Phys. Lett.* **1991**, *94*, 5865−74.

(20) Klose, S. Ph.D. Thesis, Universität Hannover, 1996.

(21) Landolt-Börnstein: *Numerical Data and Functional Relationships in Science and Technology*, New Series II/6; Hellwege, K.-H., Hellwege, A. M., Eds.; Springer: Berlin, 1974.

(22) Olsgaard, D. A.; Lasell, R. A.; Havey, M. D.; Sieradzan, A. *Phys. Rev. A.* **1993**, *48*, 1987−96.